Journal of Computational Physics 229 (2010) 7977–7996

Contents lists available at ScienceDirect

Journal of Computational Physics

journal homepage: www.elsevier.com/locate/jcp

A ghost fluid, level set methodology for simulating multiphase electrohydrodynamic flows with application to liquid fuel injection

B.P. Van Poppel *, O. Desjardins, J.W. Daily

Department of Mechanical Engineering, University of Colorado, Boulder, CO 80309, USA

ARTICLE INFO

Article history:
Received 9 February 2010
Received in revised form 24 June 2010
Accepted 2 July 2010

Keywords:
Electrohydrodynamics
Multiphase flow
Primary atomization
DNS
Ghost fluid method
Conservative level set

ABSTRACT

In this paper, we present the development of a sharp numerical scheme for multiphase electrohydrodynamic (EHD) flows for a high electric Reynolds number regime. The electric potential Poisson equation contains EHD interface boundary conditions, which are implemented using the ghost fluid method (GFM). The GFM is also used to solve the pressure Poisson equation. The methods detailed here are integrated with state-of-the-art interface transport techniques and coupled to a robust, high order fully conservative finite difference Navier–Stokes solver. Test cases with exact or approximate analytic solutions are used to assess the robustness and accuracy of the EHD numerical scheme. The method is then applied to simulate a charged liquid kerosene jet.

Published by Elsevier Inc.

1. Introduction

Electrohydrodynamics (EHD) is an interdisciplinary topic that describes the complex interaction between fluid mechanics and electric fields. EHD may enable improved spray control and finer atomization so that fuel injection schemes can be inexpensively developed for the small combustion engine class. Moreover, EHD may provide efficient enhancements to hydrocarbon fuel atomization that could benefit a much broader range of engines and even other, non-combustion applications, such as pharmaceutical coating and micro- or nano-thin-film deposition [1].

EHD is a subject that has been explored since Lord Rayleigh revealed the competing forces and resulting dynamics of a liquid drop that is radially stressed by an applied electric field in his 1882 paper [2]. Many researchers have explored EHD in multiphase systems [3–11]. A number of numerical studies have been conducted, however no reports of three-dimensional direct numerical simulations (DNS) modeling of primary atomization mechanisms for multiphase, multiphysics electrohydrodynamics have been found in the literature. Idealizations and simplifications have been employed, along with a variety of methodologies such as Lagrangian particle tracking [12,13], 2D Lattice Boltzmann methods [14], and axisymmetric Galerkin finite element methods [15]. The "leaky dielectric model" [7,16] has been employed in simulations [17].

Recent numerical work by Tomar and co-workers [18] implemented a weighted harmonic mean (WHM) interpolation scheme to smoothen the electric properties at the interface, a coupled level set and volume-of-fluid (CLSVOF) [19] algorithm for tracking the phase interface, and the continuum surface force (CSF) [20] method for the electric surface forces. In other recent work, Guildenbecher [21] reported no observed effects of electric charge on *secondary atomization* for either dielectric or conducting drops. He recommended using DNS to fully elucidate the role of electric stresses in *primary atomization* and subsequently to help develop predictive models for EHD atomization.

* Corresponding author. Tel.: +1 270 2681558; fax: +1 303 492 3498.
E-mail address: bret.vanpoppel@colorado.edu (B.P. Van Poppel).

0021-9991/$ - see front matter Published by Elsevier Inc.
doi:10.1016/j.jcp.2010.07.003

Considering the challenges and expense of experiments, high-fidelity numerical simulations should be able to provide some assistance in answering questions about the fundamentals and dynamics of EHD atomization. Its scientific promise notwithstanding, numerical simulations of realistic liquid break-up are quite challenging due to the computational expense involved. This necessitates the use of large, parallel computational resources. The long-term goals of this research effort are to understand the dynamics of EHD atomization, simulate classic experiments such as the uncharged and charged liquid kerosene jets in Fig. 1, and to pave the way for robust modeling of EHD sprays using advanced numerical methods.

In this paper, we present the development of a sharp numerical scheme for multiphase electrohydrodynamic (EHD) flows using a high electric Reynolds number assumption. The electric potential Poisson equation contains EHD interface boundary conditions, which are implemented using the ghost fluid method (GFM). The GFM is also used to solve the pressure Poisson equation. The methods detailed here are integrated within the high order fully conservative finite difference Navier–Stokes solver of the NGA code [22] which includes state-of-the-art interface transport techniques [23,24]. Test cases with exact or approximate analytic solutions are used to assess the robustness and accuracy of the EHD modules within NGA. Finally, a charged liquid kerosene jet in quiescent air is simulated and qualitatively compared to experimental results.

This paper is organized with the proceeding section presenting the analytic models and governing equations. Section 3 describes the methodology for solving the electric potential Poisson equation, and Section 4 details an efficient scheme for computing the interface boundary conditions. Section 5 describes the implementation of the Coulomb force, and Section 6 presents numerical tests used to validate the methodology. Section 7 details a three-dimensional simulation of an electrically charged kerosene jet, and a final section addresses conclusions and future work.

2. Mathematical model

In EHD flows, inertial, viscous, capillary, and electric forces are relevant and contribute to the behavior of the system. The hydrodynamic and electrostatic governing equations are summarized in this section.

Conservation of mass and momentum for a variable density, low Mach number flow are given as

$$\frac{\partial \rho}{\partial \tau} + \nabla \cdot (\rho \boldsymbol{u}) = 0, \tag{1}$$

$$\frac{\partial \rho \boldsymbol{u}}{\partial \tau} + \nabla \cdot (\rho \boldsymbol{u} \otimes \boldsymbol{u}) = -\nabla p + \nabla \cdot (\boldsymbol{\sigma}^f + \boldsymbol{\sigma}^e) + \rho \boldsymbol{g}, \tag{2}$$

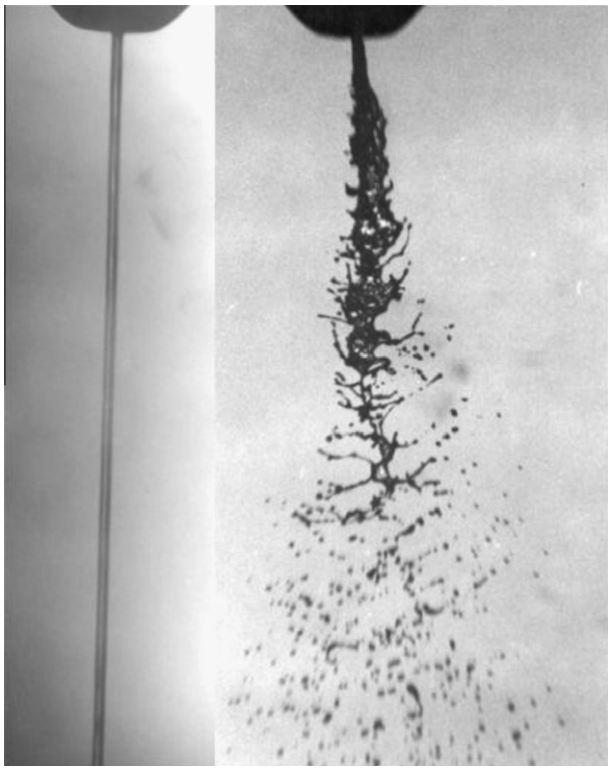

Fig. 1. Comparison of uncharged and charged kerosene jets, used with permission [12].

where $\boldsymbol{u}$ is the velocity field, p is the hydrodynamic pressure, ρ is the mass density, and $\boldsymbol{g}$ is gravitational acceleration, and τ is time. The viscous stress tensor, $\boldsymbol{\sigma}^f$, is given by

$$\boldsymbol{\sigma}^f = \mu\left(\nabla\boldsymbol{u} + \nabla\boldsymbol{u}^{\mathsf{T}}\right) - \frac{2}{3}\mu\nabla\cdot\boldsymbol{u}\mathbb{I}, \tag{3}$$

with $\mathbb{I}$ the identity tensor and μ is the dynamic viscosity. The Maxwell stress tensor, $\boldsymbol{\sigma}^e$, and the corresponding electric body force, $\boldsymbol{f}_e$, are described by

$$\boldsymbol{\sigma}^e = \epsilon\boldsymbol{E}\boldsymbol{E} - \frac{\epsilon}{2}\boldsymbol{E}\cdot\boldsymbol{E}\left(1 - \frac{\rho}{\epsilon}\frac{\partial\epsilon}{\partial\rho}\right)\mathbb{I}, \tag{4}$$

$$\boldsymbol{f}_e = \nabla\cdot\boldsymbol{\sigma}^e = q\boldsymbol{E} - \frac{1}{2}\boldsymbol{E}^2\nabla\epsilon + \nabla\left(\frac{1}{2}\rho\frac{\partial\epsilon}{\partial\rho}\boldsymbol{E}^2\right), \tag{5}$$

where ϵ is the electric permittivity, q is a volumetric electric charge density, and $\boldsymbol{E}$ is the electric field vector. The three terms of $\boldsymbol{f}_e$ represent the Coulomb force, the dielectric force, and the electrostrictive force, respectively. The electric displacement vector, $\boldsymbol{D}$, is assumed to vary linearly with the electric field vector for the incompressible and homogeneous flows considered here, as

$$\boldsymbol{D} = \epsilon\boldsymbol{E}. \tag{6}$$

The electric field vector is irrotational, a consequence of the electrostatic assumption, hence it can be expressed as the gradient of the scalar electric potential, ϕ, as

$$\boldsymbol{E} = -\nabla\phi. \tag{7}$$

The Gauss law can be employed for a dielectric material to relate the electric displacement vector to the volumetric charge, as

$$\nabla\cdot\boldsymbol{D} = \nabla\cdot\epsilon\boldsymbol{E} = -\nabla\cdot(\epsilon\nabla\phi) = q. \tag{8}$$

Henceforth, Eq. (8) will be referred to as the *electric potential Poisson equation*. The electric charge conservation equation is described by

$$\frac{\partial q}{\partial\tau} + \nabla\cdot\boldsymbol{J} = 0, \tag{9}$$

where $\boldsymbol{J}$ is the current density, which can be expressed as

$$\boldsymbol{J} = \mu_i q\boldsymbol{E} - D_i\nabla q + q\boldsymbol{u}, \tag{10}$$

where D_i is the molecular diffusion coefficient and μ_i is the ionic mobility coefficient.

While the velocity and tangential electric field components are continuous across the interface, the mass density, viscosity, and electric displacement vector experience jumps, described by

$$[\boldsymbol{u}\cdot\boldsymbol{n}]_\Gamma = 0, \tag{11}$$

$$[\boldsymbol{u}\cdot\boldsymbol{t}_i]_\Gamma = 0, \quad \text{for } i = 1,2, \tag{12}$$

$$[\rho]_\Gamma = \rho_l - \rho_g, \tag{13}$$

$$[\mu]_\Gamma = \mu_l - \mu_g, \tag{14}$$

$$[\epsilon]_\Gamma = \epsilon_l - \epsilon_g, \tag{15}$$

$$[\boldsymbol{D}]_\Gamma = \boldsymbol{n}\cdot[\epsilon\boldsymbol{E}]_\Gamma = q_s, \tag{16}$$

$$\boldsymbol{n}\times[\boldsymbol{E}]_\Gamma = 0, \tag{17}$$

where $[(\cdot)]_\Gamma$ represents the jump of "$(\cdot)$" across the interface, Γ, and for example, $[\boldsymbol{D}]_\Gamma$ represents the jump of the electric displacement vector across the interface, $\boldsymbol{n}$ and $\boldsymbol{t}$ represent the normal and tangential unit vectors at the interface, superscripts l and g represent quantities in the liquid and gas phases, respectively, and q_s the surface charge. A direct consequence of the irrotational jump condition, Eq. (17), ensures that the tangential components of the electric field, and therefore the electric potential, ϕ, are continuous,

$$[E_{t_1}]_\Gamma = 0, \quad [E_{t_2}]_\Gamma = 0, \text{ and} \tag{18}$$

$$[\phi]_\Gamma = 0. \tag{19}$$

The pressure interface jump condition includes contributions from viscous, electric and surface tension forces, and is represented as

$$-[p]_\Gamma + [\boldsymbol{n}^{\mathsf{T}}\cdot(\boldsymbol{\sigma}^e + \boldsymbol{\sigma}^f)\cdot\boldsymbol{n}]_\Gamma = -\gamma\kappa, \tag{20}$$

which can be simplified as

$$[p]_\Gamma - 2[\mu]_\Gamma \boldsymbol{n}^{\mathsf{T}} \cdot \nabla \boldsymbol{u} \cdot \boldsymbol{n} - \gamma\kappa = \left[\frac{1}{2}\epsilon E_n^2\right]_\Gamma - \left[\frac{1}{2}\epsilon E_{t_i}^2\right]_\Gamma, \tag{21}$$

where $[p]_\Gamma$ is the pressure jump across the interface, γ the surface tension coefficient, and κ the local interface curvature. The tangential shear stress balance yields

$$[\boldsymbol{n}^{\mathsf{T}} \cdot (\boldsymbol{\sigma}^e + \boldsymbol{\sigma}^f) \cdot \boldsymbol{t}_i]_\Gamma = 0. \tag{22}$$

The conservation of charge at the interface is described as [7,16,25],

$$[\boldsymbol{J} \cdot \boldsymbol{n}]_\Gamma + \nabla_s \cdot \boldsymbol{J}_s = (\boldsymbol{n} \cdot \boldsymbol{u})[q]_\Gamma - \frac{\partial q_s}{\partial t} - \boldsymbol{u}_s \cdot \nabla_s q_s + q_s \boldsymbol{n} \cdot (\boldsymbol{n} \cdot \nabla)\boldsymbol{u}, \tag{23}$$

where $\boldsymbol{J}_s$ is the surface current density, $\boldsymbol{u}_s$ the interface surface velocity, and ∇_s represents a surface gradient operator.

2.1. Modeling strategy for high electric Reynolds number

Rigorous modeling of the governing equations and interface boundary conditions presents many challenges, one of which is the accumulation of bulk volumetric charge as a surface charge in a thin electric boundary layer much smaller than the hydrodynamic boundary layer. Furthermore, the surface charge interface boundary condition, Eq. (23), is difficult to implement and its complexity is compounded by temporally and spatially varying accumulation of surface charge. Considering these challenges, it seems logical to model the disposition of the electric charge as belonging to one of two limiting regimes: either a bulk, volumetric charge or a fully relaxed surface charge.

The classic leaky dielectric model, first proposed by Taylor [26] and subsequently summarized in [7,16], is frequently used to describe the effects of electric charge in dielectric liquids. The model contends that no real dielectric is perfect, and conduction processes cannot be completely ignored. One fundamental assumption of this model is that electric charge, however introduced into a dielectric liquid, has sufficient time to fully relax from a bulk volumetric charge to a surface charge. In low-inertia systems dominated by viscosity, surface tension or both, this assumption is relevant. For inertial flows, however, the advection time scale is often the governing time scale, which in some cases can be much shorter than the space charge relaxation time scale. For a situation of unipolar space charge injected into a dielectric liquid, charge relaxation will occur as the result of mutual repulsion of like charges rather than through pure conduction processes [27]. The space charge relaxation time, τ_{sc}, represents the typical time for volumetric charge, q, to decay [28,29], and the advection time scale, τ_f, is a characteristic time for a fluid element to move a distance defined by a relevant length scale, l_o. The two time scales are described by

$$\tau_{sc} = \frac{\epsilon}{\mu_i q}, \tag{24}$$

$$\tau_f = \frac{l_o}{u}. \tag{25}$$

The electric Reynolds number, Re_e, is defined here as the ratio of charge relaxation and advection times,

$$\mathrm{Re}_e = \frac{\tau_{sc}}{\tau_f}. \tag{26}$$

For illustration, consider a liquid dielectric hydrocarbon fuel into which unipolar electric charge is injected via electrochemical processes. Numerous experiments have been conducted using this "direct charge injection" technique, most notably those performed by Lehr and Hiller [30] and Yule and co-workers [9,31–33]. Using properties for liquid kerosene and experimental parameters provided in [9] for nozzle diameter, d_o = 500 μm, injection charge, q = 0.5 C/m^3, Reynolds number, Re = 1900, and electric permittivity, $\epsilon = \kappa_e \epsilon_o$ = 1.95e−11 F/m, a time scale comparison using $l_o = d_o$ yields

$$\tau_{sc} \approx 0.039 \text{ s},$$
$$\tau_f \approx 0.00005 \text{ s},$$
$$\mathrm{Re}_e \approx 780,$$

where typical values of ion mobility, μ_i = 1e−9 m^2/V s, dielectric constant, κ_e = 2.2, and vacuum permittivity, ϵ_o = 8.854e−12 F/m, are used. The smallest characteristic electric Reynolds number would be one based on the full length of the computational domain, $\mathrm{Re}_e^* = \epsilon u / \mu_i q l_o^*$. For a domain length of $l_o^* = 20 d_o$, the corresponding electric Reynolds number would be $\mathrm{Re}_e^* \approx 40$, which suggests that a fluid particle would need to move more than 40 times the length of this computational domain before charge is fully relaxed to the surface. Given this time scale analysis, a reasonable approximation for the disposition of the electric charge is one in which the charge is "bound" and moves with the fluid velocity. In this paper, we assume constant volumetric charge and use this assumption as the foundation for the model described in the remainder of this section.

The assumption of constant volumetric space charge implies negligible surface charge. This assumption, along with incompressibility and material homogeneity within a phase, permit some simplifications of the governing equations and interface boundary conditions. Considering the electric body force, $\boldsymbol{f}_e$, given in Eq. (5), the electrostriction term can be ne-

glected [27,29]. The dielectric force appears in the pressure jump in Eq. (21), and subsequently the force density, Eq. (5), reduces to the Coulomb force in the bulk

$$\boldsymbol{f}_e = q\boldsymbol{E}. \tag{27}$$

Constant volumetric charge reduces the charge conservation equation to a solenoidal current density, described by

$$\nabla \cdot \boldsymbol{J} = 0, \tag{28}$$

and also eliminates the diffusion term in the current density, Eq. (10). For inertial flows of dielectric liquids, the ionic mobility term in Eq. (10) can be neglected for electric field strengths less than 10^7 V/m, and therefore the current density can be described as charge convecting with the fluid velocity,

$$\boldsymbol{J} = q\boldsymbol{u}. \tag{29}$$

Negligible surface charge implies that the normal component of the electric displacement vector is continuous. However, the jump in electric permittivity across the phase interface imposes a discontinuity in the normal component of the electric field, and Eq. (16) becomes

$$\boldsymbol{n} \cdot [\boldsymbol{D}]_\Gamma = \boldsymbol{n} \cdot [\epsilon \boldsymbol{E}]_\Gamma = [\epsilon E_n]_\Gamma = 0. \tag{30}$$

With negligible surface charge, constant permittivity within each phase, and negligible electrostriction, the jump in the tangential electric stress is zero, and hence Eq. (22) reduces to

$$\left[\boldsymbol{n}^{\mathrm{T}} \cdot (\boldsymbol{\sigma}^f) \cdot \boldsymbol{t}_i\right]_\Gamma = 0. \tag{31}$$

In the proceeding sections, we implement this model, employing the ghost fluid method to solve the electric potential Poisson equation and to develop a numerically sharp technique for computing the EHD pressure jump.

3. Ghost fluid method implementation for electric potential Poisson equation

Different strategies have been developed to handle the large density ratio and the surface tension force in a flow solver. The continuum surface force approach (CSF) [20] spreads out both the density jump and the surface tension force over a few cells surrounding the interface in order to facilitate the numerical discretization. Consequently, this approach tends to misrepresent the smallest front structures. In the context of finite differences, the ghost fluid method (GFM) [34] provides a very attractive way of handling discontinuities by using generalized Taylor series expansions that directly include these discontinuities, as depicted in Fig. 2. Because GFM explicitly deals with the electric permittivity jump in the electric potential Poisson equation, the resulting discretization is not affected by the permittivity ratio. The GFM is also used to handle the jump in the density ratio in the pressure Poisson equation. In this equation, the surface tension force is included directly in the form of a pressure jump, providing a sharp numerical treatment of this singular term. Given its appealing attributes, the GFM is chosen as the method to implement the electric potential Poisson equation and the EHD interface jump conditions.

An initial step in implementing an EHD module is to solve for the electric potential, ϕ, which is an additional variable coefficient Poisson equation given in Eq. (8). In previous work, a generalized Taylor series expansion was employed to provide a sharp implementation for the pressure Laplacian across an interface jump [22,23,35]. Using a similar approach, a sharp formulation is presented for the gradient and Laplacian of the electric potential, in either the gas or the liquid phase.

Using the simplification of no surface charge from Eq. (30), a convenient expression for the jump in the normal component of the electric field can be derived as

$$[\epsilon E_n]_\Gamma = [\epsilon]_\Gamma E_n^g + \epsilon_l [E_n]_\Gamma = 0. \tag{32}$$

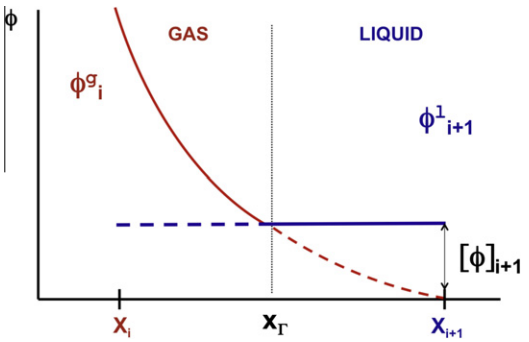

Fig. 2. Illustration of ghost fluid method for a variable, such as the electric potential, ϕ, which displays a discontinuity in its gradient, $\frac{\partial \phi}{\partial x}$, at x_Γ. Dashed lines depict Taylor series expansions across the interface and dotted line represents the interface location [35].

Hence,

$$[E_n]_\Gamma = \frac{-[\epsilon]_\Gamma}{\epsilon_l} E_n^g = \frac{(\epsilon_g - \epsilon_l)}{\epsilon_l} E_n^g = (1/\epsilon_r - 1) E_n^g, \tag{33}$$

or equivalently,

$$[E_n]_\Gamma = \frac{-[\epsilon]_\Gamma}{\epsilon_g} E_n^l = \frac{(\epsilon_g - \epsilon_l)}{\epsilon_g} E_n^l = (1 - \epsilon_r) E_n^l, \tag{34}$$

where ϵ_r is the ratio of electric permittivities. In addition, we still have continuous tangential electric field components,

$$[E_{t_1}]_\Gamma = 0 \quad \text{and} \quad [E_{t_2}]_\Gamma = 0.$$

The jump in the electric displacement vector can be written as the product of the scalar permittivity and the electric field vector, $[\boldsymbol{D}]_\Gamma = [\epsilon \boldsymbol{E}]_\Gamma$, using the previously stated assumption of electrically linear behavior. Re-arranging the jump algebraically, we can describe the product of permittivity and the electric field vector as

$$[\epsilon \boldsymbol{E}]_\Gamma = \epsilon_l [\boldsymbol{E}]_\Gamma + \boldsymbol{E}^g [\epsilon]_\Gamma, \tag{35}$$

and with the continuous tangential components, the first term on the right-hand side reduces, yielding

$$[\epsilon \boldsymbol{E}]_\Gamma = \epsilon_l [E_n] \boldsymbol{n} + [\epsilon]_\Gamma \boldsymbol{E}^g. \tag{36}$$

Expressing the jump in vector form for its Cartesian dimensions gives

$$\begin{aligned} [\epsilon \boldsymbol{E}]_\Gamma &= [\epsilon (E_x \boldsymbol{e}_x + E_y \boldsymbol{e}_y + E_z \boldsymbol{e}_z)]_\Gamma, \\ &= [\epsilon E_x]_\Gamma \boldsymbol{e}_x + [\epsilon E_y]_\Gamma \boldsymbol{e}_y + [\epsilon E_z]_\Gamma \boldsymbol{e}_z. \end{aligned} \tag{37}$$

Incorporating Eq. (36), the Cartesian components can be expressed as,

$$[\epsilon E_x]_\Gamma = \epsilon_l [E_n] (\boldsymbol{n} \cdot \boldsymbol{e}_x) + [\epsilon]_\Gamma E_x^g, \tag{38}$$
$$[\epsilon E_y]_\Gamma = \epsilon_l [E_n] (\boldsymbol{n} \cdot \boldsymbol{e}_y) + [\epsilon]_\Gamma E_y^g, \tag{39}$$
$$[\epsilon E_z]_\Gamma = \epsilon_l [E_n] (\boldsymbol{n} \cdot \boldsymbol{e}_z) + [\epsilon]_\Gamma E_z^g, \tag{40}$$

and substituting Eq. (33) yields the following for each Cartesian component,

$$[\epsilon E_x]_\Gamma = [\epsilon]_\Gamma (E_x^g - E_n^g n_x), \tag{41}$$
$$[\epsilon E_y]_\Gamma = [\epsilon]_\Gamma (E_y^g - E_n^g n_y), \tag{42}$$
$$[\epsilon E_z]_\Gamma = [\epsilon]_\Gamma (E_z^g - E_n^g n_z), \tag{43}$$

where $n_x = \boldsymbol{n} \cdot \boldsymbol{e}_x$, $n_y = \boldsymbol{n} \cdot \boldsymbol{e}_y$, and $n_z = \boldsymbol{n} \cdot \boldsymbol{e}_z$, represent the Cartesian components of the interface normal vector.

Eqs. (41)–(43) are challenging to implement within a staggered mesh numerical scheme. The electric potential, ϕ, level set, G, and interface normals are known at the cell centers, while vector quantities are computed at the faces. Direct computation of the normal electric field component, E_n, would require a very large stencil, thereby greatly increasing the cost of solving the electric potential Poisson equation.

Following the methodology proposed by Liu et al. [36], we employ a simplification that enables an efficient, dimension-by-dimension application of the jump, described by

$$[\epsilon \boldsymbol{E}]_\Gamma \approx [\epsilon E_n]_\Gamma \boldsymbol{n}. \tag{44}$$

As suggested by Liu et al. [36], this assumption accurately and efficiently captures the jump in the normal component, but leads to the generally false identity $[\epsilon E_{t_i}]_\Gamma = 0$. However, we know $[\epsilon E_{t_i}]_\Gamma = [\epsilon]_\Gamma E_{t_i}$ since $[E_{t_i}]_\Gamma = 0$. For cases of interest in this work, the normal component of the electric field vector is expected to be significantly larger than its tangential component, and therefore the error in the tangential jump is likely to remain small. The simplification described by Eq. (44) is employed only for the electric potential in order to enable an efficient solution for this variable coefficient Poisson equation.

The Cartesian components of the jump were specified in Eq. (37). Assuming the components are uniquely zero and following the methodology in Eqs. (32)–(34) yields,

$$[E_x]_\Gamma = \frac{-[\epsilon]_\Gamma}{\epsilon_l} E_x^g = \frac{(\epsilon_g - \epsilon_l)}{\epsilon_l} E_x^g = (1/\epsilon_r - 1) E_x^g, \tag{45}$$
$$[E_x]_\Gamma = \frac{-[\epsilon]_\Gamma}{\epsilon_g} E_x^l = \frac{(\epsilon_g - \epsilon_l)}{\epsilon_g} E_x^l = (1 - \epsilon_r) E_x^l. \tag{46}$$

Summarizing for all three dimensions,

$$[E_x]_\Gamma \approx (1/\epsilon_r - 1)E_x^g = (1-\epsilon_r)E_x^l, \tag{47}$$
$$[E_y]_\Gamma \approx (1/\epsilon_r - 1)E_y^g = (1-\epsilon_r)E_y^l, \tag{48}$$
$$[E_z]_\Gamma \approx (1/\epsilon_r - 1)E_z^g = (1-\epsilon_r)E_z^l. \tag{49}$$

Eqs. (47)–(49) represent an efficient set of dimension-by-dimension interface jumps. To discretize these equations, consider a Taylor series expansion of ϕ at stencil points x_i and x_{i+1}, as

$$[\phi]_i = [\phi]_\Gamma + (x_i - x_\Gamma)[\nabla\phi]_\Gamma + O((x_i - x_\Gamma)^2), \tag{50}$$
$$[\phi]_{i+1} = [\phi]_\Gamma + (x_{i+1} - x_\Gamma)[\nabla\phi]_\Gamma + O((x_{i+1} - x_\Gamma)^2). \tag{51}$$

The electric potential is continuous at the interface, guaranteed by Eq. (19). We employ the jump in the gradient, $[\nabla\phi]_\Gamma$, to provide a sharp representation for the jump in ϕ between neighboring stencil points,

$$[\phi]_i \approx (x_i - x_\Gamma)[\nabla\phi]_\Gamma, \tag{52}$$
$$[\phi]_{i+1} \approx (x_{i+1} - x_\Gamma)[\nabla\phi]_\Gamma. \tag{53}$$

Note, the jump in the electric potential gradient is equivalent to the jump in the electric field vector, $[\nabla\phi]_\Gamma = -[\boldsymbol{E}]_\Gamma$. Applying the Cartesian dimension jump in Eqs. (47)–(49) yields

$$[\nabla_x\phi]_\Gamma = -[E_x]_\Gamma = \frac{-[\epsilon]_\Gamma E_x^g|_\Gamma}{\epsilon_l}, \tag{54}$$

where,

$$E_x^g|_\Gamma \approx E_x^g|_{i+1/2} = \frac{\phi_{i+1}^g - \phi_i^g}{\Delta x} = \frac{\phi_{i+1}^l - \phi_i^g}{\Delta x} - \frac{[\phi]_{i+1}}{\Delta x}, \tag{55}$$

as depicted in Fig. 2, and therefore

$$[\phi]_{i+1} = -(x_{i+1} - x_\Gamma)\frac{[\epsilon]_\Gamma}{\epsilon_l}\left(\frac{\phi_{i+1}^l - \phi_i^g}{\Delta x} - \frac{[\phi]_{i+1}}{\Delta x}\right). \tag{56}$$

The efficient formulation described in Eqs. (54)–(56) assumes that the jump in the gradient of ϕ is constant and can be moved to a known stencil point. This shift in position may induce an error, which we expect to remain small for a slowly varying interface.

Defining a gas fraction index, $\theta = (x_\Gamma - x_i)/\Delta x$, and modified permittivity, $\epsilon^\star = \epsilon_l\theta + \epsilon_g(1-\theta)$, yields

$$[\phi]_{i+1} = \left(1 - \frac{\epsilon_l}{\epsilon^\star}\right)(\phi_{i+1}^l - \phi_i^g). \tag{57}$$

Employing the modified permittivity yields a discretized expression for the gradient of the potential, given by

$$\epsilon_g \left.\frac{\partial\phi}{\partial x}\right|_{i+1/2}^g = \epsilon_g\left(\frac{\phi_{i+1}^l - \phi_i^g}{\Delta x} - \frac{[\phi]_{i+1}}{\Delta x}\right) = \left(\frac{\phi_{i+1}^l - \phi_i^g}{\Delta x} - \left(1 - \frac{\epsilon_l}{\epsilon^\star}\right)\left(\frac{\phi_{i+1}^l - \phi_i^g}{\Delta x}\right)\right) = \frac{\epsilon_g\epsilon_l}{\epsilon^\star}\left(\frac{\phi_{i+1}^l - \phi_i^g}{\Delta x}\right). \tag{58}$$

Simplifying provides a direct expression for the gradient of the electric potential in the gas,

$$\left.\frac{\partial\phi}{\partial x}\right|_{i+1/2}^g = \frac{\epsilon_l}{\epsilon^\star}\left(\frac{\phi_{i+1}^l - \phi_i^g}{\Delta x}\right). \tag{59}$$

Recognizing that in the liquid, the gas fraction becomes $\theta = (x_{i+1} - x_\Gamma)/\Delta x$ provides a similar expression for the gradient in the liquid, described by

$$\left.\frac{\partial\phi}{\partial x}\right|_{i+1/2}^l = \frac{\epsilon_g}{\epsilon^\star}\left(\frac{\phi_{i+1}^g - \phi_i^l}{\Delta x}\right). \tag{60}$$

Extending this methodology yields a discretization for the Laplacian of the electric potential, written in either the liquid or the gas phase as

$$\left.\frac{\partial}{\partial x}\left(\epsilon_l\frac{\partial\phi}{\partial x}\right)\right|_{i+1/2}^l = \frac{\epsilon_l\epsilon_g}{\epsilon^\star}\left(\frac{\phi_{i+1}^g - \phi_i^l}{\Delta x^2}\right) - \epsilon_l\left(\frac{\phi_i^l - \phi_{i-1}^l}{\Delta x^2}\right), \tag{61}$$
$$\left.\frac{\partial}{\partial x}\left(\epsilon_g\frac{\partial\phi}{\partial x}\right)\right|_{i+1/2}^g = \frac{\epsilon_l\epsilon_g}{\epsilon^\star}\left(\frac{\phi_{i+1}^l - \phi_i^g}{\Delta x^2}\right) - \epsilon_g\left(\frac{\phi_i^g - \phi_{i-1}^g}{\Delta x^2}\right). \tag{62}$$

Eqs. (59)–(62) are implemented within the EHD module of NGA to provide a robust, efficient and accurate solution for the electric potential.

4. Sharp numerical method for EHD pressure jump

A second step to developing an EHD module is to implement a sharp, numerically accurate scheme for the EHD interface jump conditions in Eq. (21). Even with perfect dielectrics, EHD effects can be noticed due to the strong coupling through the jump conditions at the interface. The right-hand side of Eq. (21) shows how the electric stresses contribute to the pressure jump across the interface through the normal and tangential components of the electric field. In this section, we derive a mathematical formulation for the pressure jump that includes the EHD stresses, and then use the GFM to develop an efficient numerical scheme to compute the normal and tangential electric field components at the phase interface.

Considering the right-hand side of Eq. (21), we expand the EHD contributions to the overall pressure jump. Employing algebraic manipulation similar to that in Section 3 yields

$$\left[\frac{1}{2}\epsilon E_n^2\right]_\Gamma = \epsilon_l [E_n]_\Gamma \left(E_n^l + E_n^g\right) + (E_n^g)^2 [\epsilon]_\Gamma. \tag{63}$$

Combining Eqs. (33) and (63) yields

$$\left[\frac{1}{2}\epsilon E_n^2\right]_\Gamma = -[\epsilon]_\Gamma (E_n^g E_n^l). \tag{64}$$

Recognizing that the jump in the square of the tangential component, $[E_{t_i}^2]_\Gamma$, is identically zero provides a convenient simplification for the jump in the tangential field terms. Superscripts g and l are omitted since they are irrelevant for the continuous tangential components, and therefore

$$\left[\epsilon E_{t_i}^2\right]_\Gamma = E_{t_i}^2 [\epsilon]_\Gamma. \tag{65}$$

Combining Eqs. (64) and (65) to form the right-hand side of Eq. (21) yields

$$\left[\frac{1}{2}\epsilon E_n^2\right]_\Gamma - \left[\frac{1}{2}\epsilon E_{t_1}^2\right]_\Gamma - \left[\frac{1}{2}\epsilon E_{t_2}^2\right]_\Gamma = \frac{-[\epsilon]_\Gamma}{2}\left(E_n^g E_n^l + (E_{t_1})^2 + (E_{t_2})^2\right). \tag{66}$$

The quantity $E_n^g E_n^l$ is challenging to evaluate. This product can be re-cast in terms of either the gas or liquid side, as

$$E_n^g E_n^l = \begin{cases} (E_n^g)^2 \frac{1}{\epsilon_r} & \text{(gas side)}, \\ (E_n^l)^2 \epsilon_r & \text{(liquid side)}. \end{cases} \tag{67}$$

Combining Eqs. (66) and (67) and Eq. (21) yields a final form of the pressure jump, which accounts for EHD, viscous, and surface tension stresses,

$$[p]_\Gamma - 2[\mu]_\Gamma \boldsymbol{n}^{\mathrm{T}} \cdot \nabla \boldsymbol{u} \cdot \boldsymbol{n} - \gamma\kappa = \begin{cases} \frac{(\epsilon_g - \epsilon_l)}{2}\left((E_n^g)^2 \frac{1}{\epsilon_r} + (E_{t_1})^2 + (E_{t_2})^2\right) & \text{(gas)}, \\ \frac{(\epsilon_g - \epsilon_l)}{2}\left((E_n^l)^2 \epsilon_r + (E_{t_1})^2 + (E_{t_2})^2\right) & \text{(liquid)}. \end{cases} \tag{68}$$

To implement the pressure jump, $[p]_\Gamma$, in Eq. (68), the normal and tangential components of the electric field are required. The interface normal vectors are known at the cell centers and the Cartesian components of the electric field are known at the cell faces, presenting a challenge for direct computation of the normal and tangential electric field components. Therefore, it is necessary to interpolate the Cartesian components of the electric field to the cell center across the phase interface, re-construct a cell-centered electric field vector, and subsequently partition the vector into normal and tangential components. The normal component of the electric field experiences a jump across the interface, and the GFM is employed to handle this discontinuity.

The jump in the electric field can be written in vector form,

$$\begin{aligned} [\boldsymbol{E}]_\Gamma &= [(E_n \boldsymbol{n} + E_{t_1} \boldsymbol{t}_1 + E_{t_2} \boldsymbol{t}_2)]_\Gamma, \\ &= [E_n]_\Gamma \boldsymbol{n} + [E_{t_1}]_\Gamma \boldsymbol{t}_1 + [E_{t_2}]_\Gamma \boldsymbol{t}_2. \end{aligned} \tag{69}$$

Incorporating the continuous tangential electric field jump condition given in Eq. (18) simplifies Eq. (69) to

$$[\boldsymbol{E}]_\Gamma = [E_n]_\Gamma \boldsymbol{n}. \tag{70}$$

The Cartesian components of the jump can be derived,

$$[E_x]_\Gamma = [\boldsymbol{E}]_\Gamma \cdot \boldsymbol{e}_x = [E_n]_\Gamma \boldsymbol{n} \cdot \boldsymbol{e}_x = [E_n] n_x, \tag{71}$$

$$[E_y]_\Gamma = [E_n] n_y, \tag{72}$$

$$[E_z]_\Gamma = [E_n] n_z. \tag{73}$$

Combining with Eqs. (33) and (34) gives

$$[E_x]_\Gamma = (1/\epsilon_r - 1)E_n^g n_x = (1-\epsilon_r)E_n^l n_x, \tag{74}$$

$$[E_y]_\Gamma = (1/\epsilon_r - 1)E_n^g n_y = (1-\epsilon_r)E_n^l n_y, \tag{75}$$

$$[E_z]_\Gamma = (1/\epsilon_r - 1)E_n^g n_z = (1-\epsilon_r)E_n^l n_z. \tag{76}$$

Eqs. (74)–(76) are used to interpolate the electric field components to the cell center.

For the stencil shown in Fig. 3, the interpolation scheme depends on whether the cell center is in the liquid or the gas phase. Since the electric field vector components are computed at the cell faces, it is also necessary to determine the phase at the cell faces. To determine whether the cell face is in the liquid or gas, the value of the level set function is interpolated to the cell face between neighboring cell centers.

Beginning with general expressions for a cell center point in the liquid or the gas phase, a second-order accurate interpolation for the electric field with a first-order approximation for the jump can be written as

$$E_x|^l_{i+1/2} = \frac{E^l_{x,i} + E^l_{x,i+1}}{2} = \frac{E^l_{x,i} + E^g_{x,i+1}}{2} + \frac{[E_x]_\Gamma}{2}, \tag{77}$$

$$E_x|^g_{i+1/2} = \frac{E^g_{x,i} + E^g_{x,i+1}}{2} = \frac{E^g_{x,i} + E^l_{x,i+1}}{2} - \frac{[E_x]_\Gamma}{2}. \tag{78}$$

Since the interface normal is known at the cell center, we use the formulation in Eqs. (71)–(73) to accurately represent each Cartesian component of the jump. Combining with Eqs. (77) and (78) yields a dimension by dimension expression for the electric field jump at the cell center. Written only in the x-component for brevity, but in both the liquid and gas phase, gives

$$\left[E^l_x\right]_{\Gamma,(i+1/2)} = (1-\epsilon_r)(E_{x,i+1/2}n_x + E_{y,j+1/2}n_y + E_{z,k+1/2}n_z)^l n_x, \tag{79}$$

$$[E^g_x]_{\Gamma,(i+1/2)} = \left(\frac{1}{\epsilon_r} - 1\right)(E_{x,i+1/2}n_x + E_{y,j+1/2}n_y + E_{z,k+1/2}n_z)^g n_x. \tag{80}$$

For simplicity, we introduce a coefficient, $C^{l,g}_{x,y,z}$, to represent the jump conditions for one or two jumps within a cell for each Cartesian dimension. With superscripts l and g representing the liquid and gas phases at the cell center, respectively, the coefficient is described as

$$C^{l,g}_{x,y,z} = \begin{cases} 0 & \text{if no jump,} \\ (1-\epsilon_r) & \text{single jump, liquid at cell center,} \\ (1-1/\epsilon_r) & \text{single jump, gas at cell center,} \\ 2(1-\epsilon_r) & \text{double jump, liquid at cell center,} \\ 2(1-1/\epsilon_r) & \text{double jump, gas at cell center.} \end{cases} \tag{81}$$

Re-writing Eqs. (79) and (80), and accounting for the sign difference (+/−) of Eqs. (77) and (78) yields

$$E_x|^l_{i+1/2} = \frac{E^l_{x,i} + E^g_{x,i+1}}{2} + \frac{C^l_x(E_x|^l_{i+1/2}n_x + E_y|^l_{j+1/2}n_y + E_z|^l_{k+1/2}n_z)n_x}{2}, \tag{82}$$

$$E_x|^g_{i+1/2} = \frac{E^l_{x,i} + E^g_{x,i+1}}{2} + \frac{C^g_x(E_x|^g_{i+1/2}n_x + E_y|^g_{j+1/2}n_y + E_z|^g_{k+1/2}n_z)n_x}{2}. \tag{83}$$

This methodology is extended in three dimensions to yield a representation for the electric field interpolated to the cell center. The cell-centered electric field is partitioned into normal and tangential components, which are used to compute the

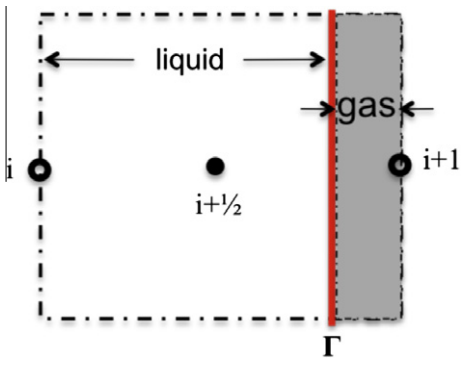

Fig. 3. x-Stencil shows interface location; gas fraction, θ, less than 50%.

right-hand side of the pressure jump in Eq. (21) at the cell center. The pressure jump is linearly interpolated to the interface and then used to solve the pressure Poisson equation, which also employs the GFM [23,24].

5. Implementation of coulomb force

The Coulomb force, Eq. (27), is implemented as a face-centered source term in the Navier–Stokes equations. For each Cartesian dimension, charge is computed at each cell face using a height function of the liquid volume fraction according to Eq. (84), and then multiplied by the local face value of the electric field. The height function, $\lambda_{i+\frac{1}{2}j,k}$, is defined by

$$\lambda_{i+\frac{1}{2}j,k} = \begin{cases} 1 & \text{if } G_{i,j,k} \text{ and } G_{i+1,j,k} \geqslant 0, \\ 0 & \text{if } G_{i,j,k} \text{ and } G_{i+1,j,k} < 0, \\ \frac{G^{+}_{i,j,k}+G^{+}_{i+1,j,k}}{|G_{i,j,k}|+|G_{i+1,j,k}|} & \text{otherwise}, \end{cases} \tag{84}$$

where $G^{+}_{i,j,k} = \max(G_{i,j,k}, 0)$, and $G_{i,j,k}$ is the value of the level set function.

6. Validation and numerical results

Several canonical test cases were employed to validate the numerical solutions for the electric field: a one-dimensional rectangle with a flat interface separating regions of two permittivities; a one-dimensional interface with constant charge density; a charged droplet in an applied electric field accelerating to terminal velocity; a dielectric drop in a uniform electric field; and a deforming dielectric spheroid stressed by an electric field.

All simulations performed in this work employ an in-house code named NGA, for which the numerical methods presented here have been implemented in parallel using Message Passing Interface (MPI). NGA extends the family of high order fully conservative finite difference schemes proposed by Morinishi and Vasilyev [37–39] to variable density low-Mach number flows [22,35]. For all simulations in this work, second-order accurate versions of numerical schemes are employed as we expect accuracy to be limited by the GFM. NGA provides excellent accuracy and numerical robustness since its schemes discretely conserve mass, momentum, and kinetic energy away from the interface.

To fully capture liquid break-up, the NGA code employs state-of-the-art interface transport techniques, the first of which is called Spectrally Refined Interface (SRI). The SRI method achieves local refinement in the form of quadrature points in each grid cell that contains the phase-interface, so that the level set function can be reconstructed using high order polynomials, thereby providing spectral accuracy [24]. Consequently, the local numerical errors in interface transport are reduced by the combined effect of increased resolution and increased order of accuracy. To render this method computationally efficient, the transport of the level set function is performed using a semi-Lagrangian technique, removing all constraints on the time step size. Increased spatial resolution is achieved without noticeably reducing the time step size for level set transport, which is a unique feature of this method. Level set based methods usually show good accuracy, but suffer from poor mass conservation properties. By increasing the local resolution of the level set function, this new approach reduces numerical errors, thereby limiting mass conservation errors [24,40,41].

A second interface transport technique, known as Accurate Conservative Level Set (ACLS) [23], is based on the conservative level set technique introduced in Olsson and Kreiss [42]. By employing a hyperbolic tangent level set function that is transported and re-initialized using fully conservative numerical schemes, mass conservation issues that are known to affect level set methods are greatly reduced. The overall robustness of the numerical approach is increased by computing the interface normals from a signed distance function reconstructed from the hyperbolic tangent level set by a fast marching method [23]. In this paper, the ACLS method is used for simulations of atomizing liquid jets in Section 7 to leverage its excellent mass conservation qualities with the accompanying severe interface topology changes. For all other simulations, the SRI method is used to capitalize on in its exceptional accuracy.

An efficient and robust Poisson solver is essential to the performance of an incompressible CFD code. It is typical for the Poisson solver to account for 60% or more of the time spent per time step. Incorporating electrostatic effects adds an additional variable coefficient Poisson equation, thereby increasing the cost of an already expensive simulation. A recent study evaluated several solvers, including Krylov-based solvers such as preconditioned conjugate gradient, deflated conjugate gradient, and multigrid solvers such as algebraic, geometric, and matrix-based multigrid for problems similar to multiphase flows [43]. The study concluded that the black-box multigrid (BBMG) solver of Dendy [44] is the most robust and efficient method. Based on this evaluation, the choice was made to implement a BBMG solver in NGA. The implementation follows the three-dimensional description introduced in Dendy [44]. The BBMG was introduced as a preconditioner to a conjugate gradient solver. The full solver, referred to henceforth as PCG–BBMG, is ideally suited for efficiently solving the pressure and electric potential Poisson equations. The PCG–BBMG solver was employed for all the test cases discussed in this paper.

6.1. Horizontal interface

The analytic solution for a horizontal, flat interface in an electric field was initially used to validate the Poisson solver for the electric potential. As depicted in Fig. 4, the domain is rectangular of height L with Dirichlet boundary conditions for the

potential, set to a constant value on top of the domain, ϕ_o, and zero at the bottom. The phase interface is located at H. Above the interface, the permittivity is ϵ_l and below ϵ_g with $\epsilon_l > \epsilon_g$. The analytic solution for the electric fields above and below the interface is

$$E^l = \frac{\phi_o}{(L-H) + \left(\frac{\epsilon_l}{\epsilon_g}\right)H} \quad \text{and} \quad E^g = \frac{\phi_o}{\left(\frac{(L-H)}{(\epsilon_l/\epsilon_g)} + H\right)}. \tag{85}$$

Fig. 5 shows computational results for one representative test case where $L = 1$, $\epsilon_r = 5$, $\phi_o = 100$, and $H = 0.4$, with $n = 60$ mesh points across the domain. The ghost fluid method provides a sharp and accurate solution for the electric field, and the error for this test case is zero to machine accuracy. This result is expected because the electric field in this case is constant in each phase, the jump in the electric field is both constant and normal to the interface, and therefore the implemented GFM scheme is exact.

6.2. Horizontal interface with charge density

The analytic solution for a horizontal, flat interface with charge density is used to validate the PCG–BBMG Poisson solver for a case with a non-zero right-hand side. The geometry is the same as in the preceding example discussed in Section 6.1 and Fig. 4. The upper region, representing the liquid, maintains a constant volumetric charge, q_o. The analytic solution for the liquid is governed by Poisson's equation, while the charge-free gas region is governed by the Laplace equation, as

$$\frac{d^2\phi^l}{dy^2} = q_o \quad \text{and} \quad \frac{d^2\phi^g}{dy^2} = 0, \tag{86}$$

with the electric field in the liquid and gas described by

$$E^l(y) = \frac{qy}{\epsilon_l} - \beta \quad \text{and} \quad E^g = \epsilon_r\left(\frac{qH}{\epsilon_l} - \beta\right), \tag{87}$$

where

$$\beta = \frac{\phi_o + ql^2/(2\epsilon_l) + \epsilon_r qH^2/\epsilon_l - qH^2/(2\epsilon_r)}{L - H + \epsilon_r H}. \tag{88}$$

The simulation parameters are the same as the uncharged horizontal interface test case. The value of q_o is chosen such that the ratio of charge to applied potential is unity. Fig. 6 shows computational results for this case, illustrating excellent agreement of simulation and theory. Table 1 reports the normalized error in the y-direction electric field for this test case, showing second-order convergence with mesh refinement.

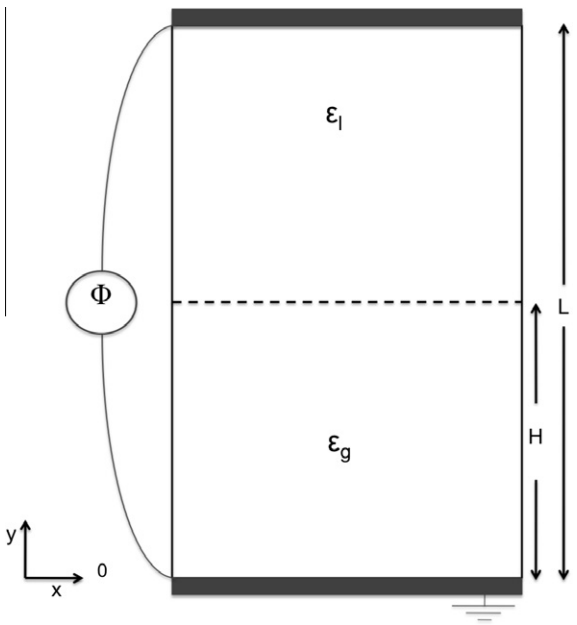

Fig. 4. Schematic for the flat, horizontal interface case.

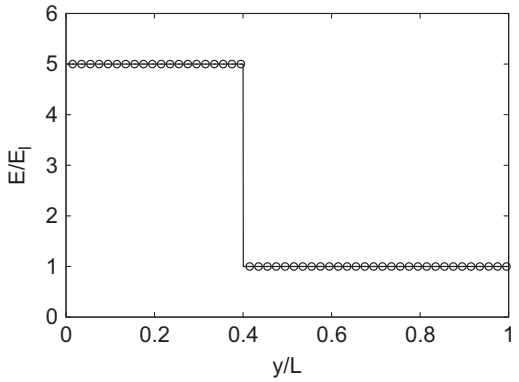

Fig. 5. Distribution of normalized electric field normal to interface for horizontal interface test case. Symbols represent simulation, solid line represents theory.

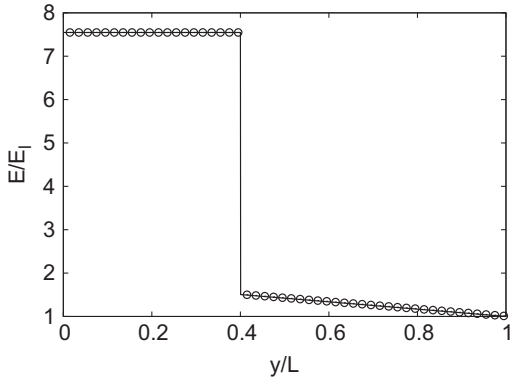

Fig. 6. Distribution of normalized electric field for charged horizontal interface test case. Symbols represent simulation, solid line represents theory.

6.3. Motion of a small charged droplet

A small point charge in a uniform electric field accelerates due to the Coulomb force, $\boldsymbol{f}_e = q\boldsymbol{E}$. In an attempt to reproduce this behavior, a small, spherical, charged droplet is placed in a uniform electric field. If the drop charge is small relative to the applied field, the spherical drop will not modify the electric field significantly, while feeling the effect of the Coulomb force. Provided that the Reynolds number is small enough, the droplet will also experience Stokes drag and will eventually reach a terminal velocity. Although a simple case, the charged drop test case evaluates the accuracy of the Coulomb force, as well as the interaction of the electric and viscous forces.

With the previous assumptions, the motion of the charged drop is governed by the ordinary differential equation

$$V_l q E_y - 6\pi\mu_g R_o \frac{dy}{d\tau} = \rho_l V_l \frac{d^2 y}{d\tau^2}, \tag{89}$$

where V_l represents the liquid volume and R_o the drop radius. The corresponding terminal velocity, u_τ, and time scale, τ^* are given as

$$u_\tau = \frac{V_l q E_y}{6\pi\mu_g R_o} \quad \text{and} \quad \tau^* = \frac{R_o}{u_\tau}. \tag{90}$$

The relevant simulation parameters include the ratio of space charge to electric field strength, $Q_E = qR_o/\epsilon E_o$, set to a value of 0.4, the viscosity ratio and density ratio to 10, the surface tension, $\gamma = 0.2$, ratio of permittivities, $\epsilon_r = 1$, and domain size of $10R_o \times 20R_o$. To limit temporal errors, the CFL is kept constant at 0.1. Fig. 7 shows the velocity of the drop over time as it accelerates to terminal velocity for three levels of mesh refinement. Simulation results are compared to the theoretical solution for Eq. (89). The normalized error of simulation compared to theory at $\tau/\tau^* = 3$ converges on mesh refinement: 11% at $R_o/h = 3$; 2.2% at $R_o/h = 6$; and 0.4% at $R_o/h = 9$, where R_o/h represents the number of grid cells across the drop radius, thereby demonstrating good convergence and excellent accuracy even with coarse resolution. The drop remains spherical throughout the simulation.

Table 1
Normalized error in y-direction electric field for a horizontal interface with charge density.

Mesh	err E_y	Order
50	1.1e−5	–
100	2.7e−6	2.02
200	6.8e−7	1.98

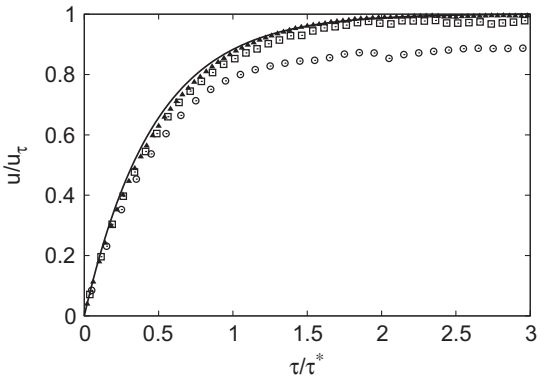

Fig. 7. Simulation of charged drop accelerating to terminal velocity. $R_o/h = 3$ (circles), $R_o/h = 6$ (squares), $R_o/h = 9$ (triangles) compared to theory (line).

6.4. Dielectric drop in a uniform electric field

For a subsequent test case, we demonstrate a three-dimensional dielectric sphere placed in a uniform electric field. The drop is ideally suited to assess the accuracy and robustness of the EHD module. Spherical shapes are commonly observed in atomization processes and represent a canonical geometry for fuel injection applications. Additionally, the electric potential at the interface decays with r^{-2} and the electric field experiences large jumps proportional to the relative permittivity, ϵ_r. Since we explicitly address the jump conditions with the GFM approach, we expect this approach to accurately capture the physical phenomena with only a few grid points across the drop radius.

The analytic solution is provided in several references [45,46] and has been demonstrated in other work as a representative test case to validate numerical methods [18,17]. In this case we compare the numerical simulation result of the pressure in a spherical drop with the analytic prediction. The geometry is shown in Fig. 8. The electric field, E_o, is applied in the y-direction far away from the sphere. Since this case assumes a perfect dielectric, the environment is free of charge, and therefore the governing equation is Laplace's equation with appropriate boundary conditions. Superscripts l and g represent regions inside and outside the drop, respectively, and specifically ϕ^l is the potential inside the drop. The permittivities are known with $\epsilon_l > \epsilon_g$ and therefore the ratio of permittivities $\epsilon_r > 1$. The analytic solutions for the electric potential and magnitude of the electric field components are

$$\phi^l(r,\theta) = E_o r\left(\frac{-3}{\epsilon_r+2}\right)\sin\theta, \tag{91}$$

$$\phi^g(r,\theta) = -E_o r\sin\theta + \left(\frac{\epsilon-1}{\epsilon+2}\right)E_o\frac{R^3}{r^2}\sin\theta, \tag{92}$$

$$E^l_{t,r=R_o} = E^g_{t,r=R_o} = \left(\frac{3E_o}{\epsilon_r+2}\right)\cos\theta, \tag{93}$$

$$E^l_{n,r=R_o} = \left(\frac{3E_o}{\epsilon_r+2}\right)\sin\theta, \text{ and} \tag{94}$$

$$E^g_{n,r=R_o} = \epsilon_r\left(\frac{3E_o}{\epsilon_r+2}\right)\sin\theta. \tag{95}$$

The pressure jump across the drop is given by

$$[p]_\Gamma = \frac{2\gamma}{R} + \frac{1}{2}\left(\frac{3E_o}{\epsilon_r+1}\right)^2\left[\epsilon_l(1-\epsilon_r)\sin^2\theta + \epsilon_g(1-\epsilon_r)\cos^2\theta\right]. \tag{96}$$

A simulation is conducted with the electric Bond number, $N_E = \epsilon E_o^2 R_o/\gamma = 0.33$, $\epsilon_r = 10$, density and viscosity ratios set to unity, drop radius $R_o = 0.1$, and surface tension, $\gamma = 0.32$ for various levels of mesh refinement on a domain of $10R_o \times 20R_o$. Results for the convergence of the y-component of the electric field at two circumferential locations are reported in Table

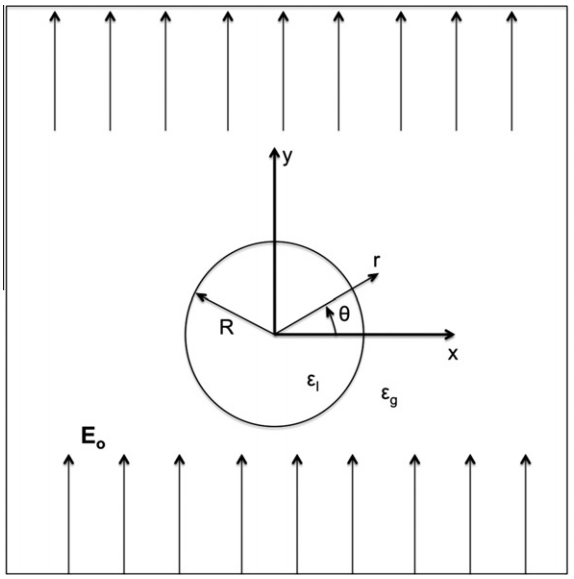

Fig. 8. Schematic for dielectric cylinder in a uniform electric field test case.

2. The electric field at the cell center is very accurate at the pole and the equator, points where the field is exclusively defined by either the normal or the tangential component. At both points, the electric field shows reasonable convergence, with the error decaying between first- and second-order with mesh refinement. Table 3 reports the convergence of the electric potential at all grid points in the neighborhood of the interface, which is defined by a sign change in the level set function compared to a neighboring cell in any direction. The electric potential shows limited convergence, remaining below first-order accuracy. These results are expected, since, as mentioned in Section 3, the numerical scheme is true to the normal jump in the electric displacement vector, $[\epsilon E_n]_\Gamma$, but smears the tangential jump, $[\epsilon E_{t_i}]_\Gamma$. Similar observations and rates of convergence were reported by Liu et al. [36]. It should also be noted that the choice of the GFM methodology represents an exchange of convergence for accuracy. In modeling multiphase and atomization processes, with characteristically small structures, numerical accuracy is expected to be the more important property.

Fig. 9 compares the simulation results to the analytic prediction of Eq. (96) for the pressure jump at the surface of the drop. The pressure jump is obtained across the sharp interface after one time step, prior to any deformation, and computed results show reasonable agreement with theory. At the equator, $\theta = 0°$, the electric field is tangential to the interface, and Fig. 9 shows reduced accuracy at this point, which might be related to tangential smearing. Table 4 shows the accuracy of the pressure jump at the equator, $\theta = 0°$, which is the point of the maximum pressure jump. The GFM scheme shows improvements in the accuracy of the pressure jump even with coarse resolution compared to previous work, such as the results reported for the same problem by Tomar et al. [18].

6.5. Deforming spheroidal drop

A number of researchers have explored the case of a suspended drop in a uniform electric field, including Taylor [10], Landau and Lifshitz [46], Cheng and Chaddock [47], Sozou [48], Baygents and Rivette [17,49], and Tomar et al. [18]. For this case, the geometry and electric field alignment are identical to that for the dielectric drop in the preceding section, as shown in Fig. 8. A spherical drop deforms when stressed by an externally applied electric field. A dielectric drop always deforms into a prolate spheroid with the major axis aligned with the electric field.

The eccentricity, e, depolarization constant, n, and the electric field inside the spheroidal drop are given by Landau and Lifshitz [46]

Table 2
Normalized error in y-direction electric field at the pole and equator of a dielectric drop.

R_o/h	err, $\theta = 0°$	Order	err, $\theta = 90°$	Order
5	2.3%	–	2.0%	–
10	0.8%	1.5	2.8%	–
20	0.4%	1.0	0.7%	2.0

Table 3
Convergence for electric potential, ϕ, at the interface of a dielectric drop.

R_o/h	L_2	Order	L_∞	Order
5	0.0137	–	0.0777	–
10	0.0086	0.67	0.0748	0.06
20	0.0061	0.50	0.0551	0.44

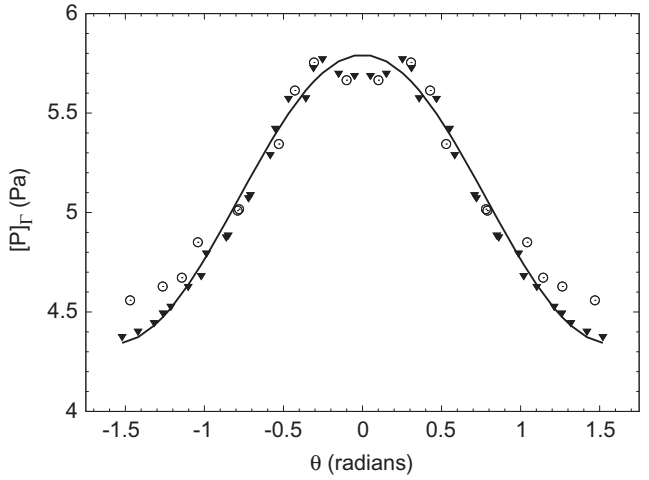

Fig. 9. Pressure jump at the interface of a dielectric cylinder. Simulation results for $R_o/h = 4$ (circles), $R_o/h = 8$ (filled triangles) compared to analytic solution (line).

Table 4
Normalized error in pressure jump at equator ($\theta = 0°$) for a dielectric drop in uniform electric field.

	R_o/h	err $[p]_\Gamma$ (%)	Order
NGA EHD	4	2.12	–
NGA EHD	8	1.03	1.09
NGA EHD	16	0.63	0.71
Tomar et al. [18]	20	4.49	–
Tomar et al. [18]	40	2.24	1.00
Tomar et al. [18]	80	1.15	0.96

$$
\begin{aligned}
e &= \sqrt{1 - a^2/b^2}, \\
n &= \frac{(1-e^2)}{(2e^3)}\left(\ln\left(\frac{(1+e)}{(1-e)}\right) - 2e\right), \\
E_l &= \frac{E_o}{(1-n) + n\epsilon_r}.
\end{aligned}
\tag{97}
$$

The force balance at the interface is

$$
[p]_\Gamma = \gamma\kappa + \frac{\epsilon_g}{2}\left(\epsilon_r (E_n^l)^2 - (E_n^g)^2 + E_t^2(1-\epsilon_r)\right). \tag{98}
$$

Considering two particular points, the *equator* ($x = a$) and the *pole* ($y = b$), the mean curvature, κ, is defined by the two principal radii of curvature, R_1 and R_2. For a prolate spheroid, these radii of curvature are given by

$$
R_1 = a^2 b^2 \left(\frac{x^2}{a^4} + \frac{y^2}{b^4}\right)^{3/2} \quad \text{and} \quad R_2 = a^2 \left(\frac{x^2}{a^4} + \frac{y^2}{b^4}\right)^{1/2}. \tag{99}
$$

The mean curvature at the end of the major axis (*i.e.* at the pole) and the curvature at the end of the minor axis (*i.e.* at the equator) are given by Taylor [10] as

Table 5
Dielectric drop in uniform electric field. Comparison of simulation with Tomar et al. [18] for computed equilibrium pressure jump at different levels of mesh refinement. Simulation L_1 and L_2 errors compared to theoretical predictions of Taylor [10], Landau and Lifshitz [46], and Cheng and Chaddock [47].

	R_o/h	$L_1\ \Delta p$	Order	$L_2\ \Delta p$	Order
NGA EHD	3	0.029	–	0.09	–
NGA EHD	6	0.004	3.00	0.03	1.63
Tomar et al. [18]	4	0.145	–	0.22	–
Tomar et al. [18]	8	0.073	0.99	0.05	2.13

$$R_1^{-1} + R_2^{-1} = \begin{cases} \frac{2b}{a^2} & \text{at the pole,} \\ \frac{a}{b^2} + \frac{1}{a} & \text{at the equator.} \end{cases}$$

The electric stress at the pole is due exclusively to the normal component (E_n); similarly the electric stress at the equator is due only to the tangential component (E_t). The tangential component is continuous at the equator, that is $E_t = E_t^l = E_t^g$ at $\theta = 0°$. Therefore the pressure jump at these locations can be expressed as

$$[p]_\Gamma = \begin{cases} \gamma\left(\frac{2b}{a^2}\right) + \frac{\epsilon_g}{2}\left(\epsilon_r (E_n^l)^2 - (E_n^g)^2\right) & \text{at the pole,} \\ \gamma\left(\frac{a}{b^2} + \frac{1}{a}\right) + \frac{\epsilon_g}{2}\left(E^l)^2(1 - \epsilon_r\right) & \text{at the equator.} \end{cases} \tag{100}$$

Simulation parameters are based upon Cheng and Chaddock's stability analysis [47] and reported in Tomar et al. [18]: $N_E = 0.49$, minor axis $r_a = R_o/1.2$, major axis $r_b = 1.44R_o$, $[p]_\Gamma = 4.24$ Pa, $R_o = 0.1$, $\gamma = 0.32$, $\epsilon_r = 10.0$, and density and viscosity ratios of unity. The domain size used is $10R_o \times 20R_o$. To limit temporal errors, the CFL is kept constant at 0.1.

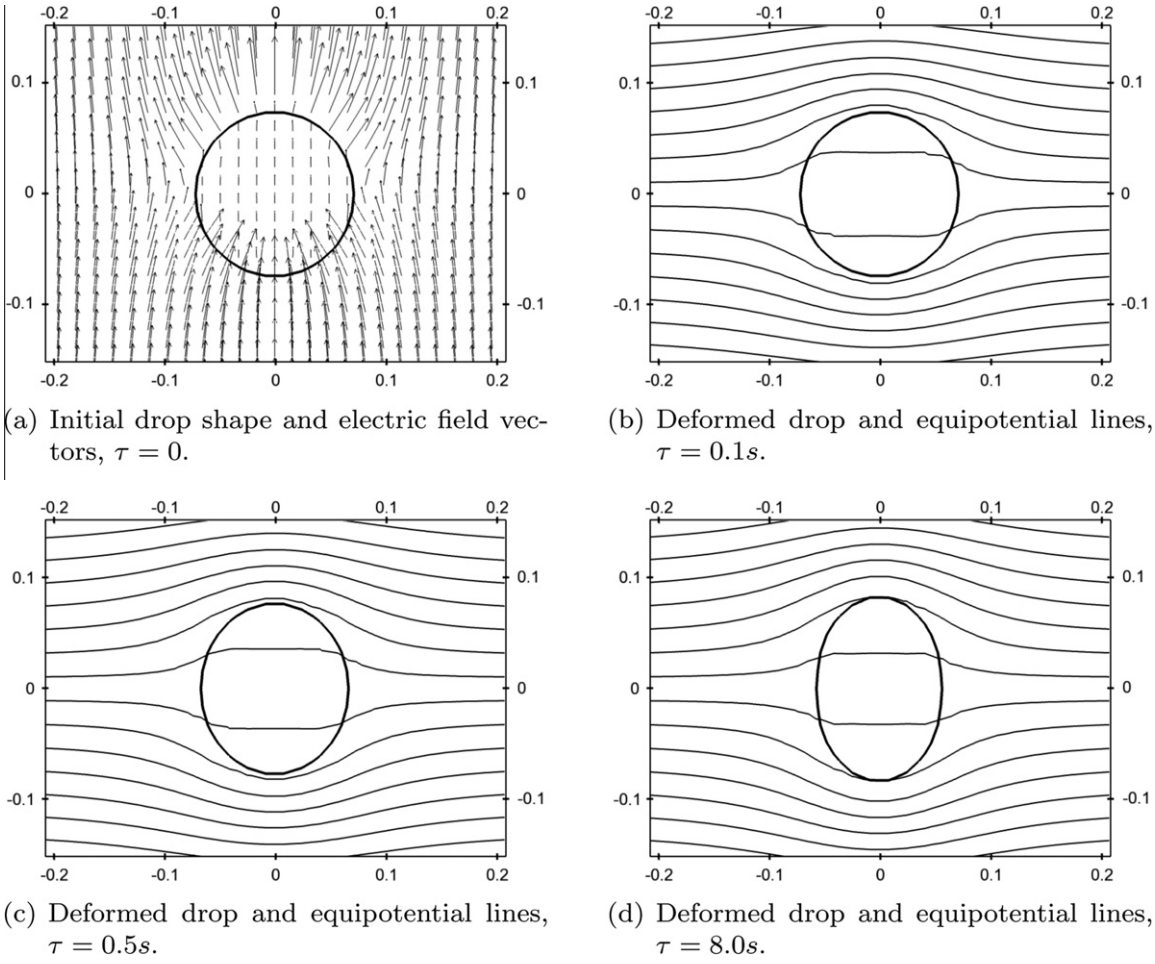

(a) Initial drop shape and electric field vectors, $\tau = 0$.

(b) Deformed drop and equipotential lines, $\tau = 0.1s$.

(c) Deformed drop and equipotential lines, $\tau = 0.5s$.

(d) Deformed drop and equipotential lines, $\tau = 8.0s$.

Fig. 10. Evolution of a deforming, dielectric drop stressed by a uniform electric field.

Table 6
Parameters for charged and uncharged liquid kerosene jet. Total mesh size is 50.3 million grid points; d_o/h represents number of grid points across nozzle diameter.

Parameter	Uncharged	Charged	Experiment
N_E	0	70	19
N_{ei}	0	1.25	0.09
q [C/m^3]	0	4	0.5
Re	2000		4900
We	850		1700
d_o [μm]	250		500
d_o/h	36		n/a
ρ_l/ρ_g	652		
μ_l/μ_g	56		
ϵ_r	2.2		
γ [N/m]	0.0235		

Results for the equilibrium drop pressure using the NGA EHD module are compared to results from previous work in Table 5. Equilibrium pressure is computed as a volume average of all cells with a liquid volume fraction of 0.99 or greater. The NGA EHD module again shows good accuracy with few grid points. Fig. 10 depicts the evolution of an initially spherical dielectric drop deforming into a prolate spheroid under the stress of an applied electric field, showing a smooth interface and iso-contours of electric potential.

7. Simulation of electrically charged liquid kerosene jet

The validation cases presented heretofore are very limited in terms of complexity, covering flows governed by surface tension and viscous effects. In order to assess the performance of the proposed approach and demonstrate its robustness,

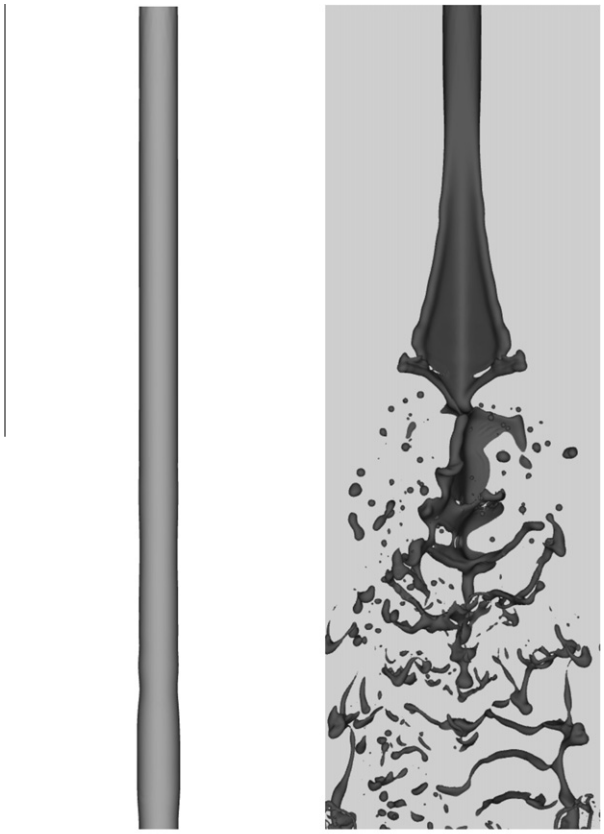

(a) Uncharged simulation. (b) Charged simulation.

Fig. 11. Comparison of uncharged and charged simulations of liquid kerosene jet.

Table 7
Proportion of time taken by each solver for each time step for a charged liquid kerosene jet simulation. The multiphase step in this simulation includes the computational time for the electric potential Poisson solver.

Multiphase including EHD	44%
Velocity	12%
Pressure	42%
Other	2%

charged and uncharged liquid jets in quiescent air are simulated. A charge injection scheme is modeled, similar to that investigated by many researchers elsewhere [33,9,5,6,30,50]. The properties for the simulation are inspired by charge injection experiments performed by Shrimpton and co-workers [9,31–33]. Parameters employed in both simulations are summarized in Table 6, with the electro-inertial number defined by $N_{ei} = q^2 d_o^2/\epsilon\rho u^2$.

Both charged and uncharged simulations correspond to a fast liquid jet of kerosene injected from a circular port of diameter d_o into quiescent air. For the charged simulation, we use a domain size of $L_x = 21d_o$, and $L_y = L_z = 7d_o$ discretized on a $768 \times 256 \times 256$ mesh. The boundary conditions implemented for this simulation are a Dirichlet condition at the upstream x-face specifying bulk inflow, a convective outflow [51] on the downstream x-face, and zero electric potential on the y- and z-faces. The interface is initialized as a liquid cylinder spanning the domain. In Fig. 11, the uncharged and charged simulations are shown side-by-side for comparison. As expected, the uncharged simulation shows no disruption or break-up. Compared to the charged experiment shown in Fig. 1, the charged simulation employs a higher level of volumetric charge, q, to enhance liquid break-up in the absence of flow disturbances. In the charged simulation, many complex phenomena interact, resulting in a liquid break-up into ligaments and drops. The presence of numerous ligaments oriented radially outward from the axial centerline bears strong resemblance to the experiment photograph, Fig. 1. The radial orientation of liquid structures is attributable to Coulombic repulsion that arises from the space charge field, and is similar to that discussed elsewhere, for example in [52]. Coulombic repulsion leads to an electric field oriented radially from the liquid core. The Coulomb force is, therefore, a disruptive force that gives rise to the shape and orientation of the structures dislodged from the liquid core. The presence of spherical drops is attributable to surface tension forces, which become more significant for smaller structures. A more detailed assessment of liquid break-up mechanisms will be reported in a future publication.

The charged simulation requires 70% more computational time than an uncharged jet. The addition of the electric potential Poisson equation and a complex space charge electric field account for the increase in computational expense in the charged simulation. Table 7 reports the proportion of time per time step required for each of the major computational components for the charged simulation using the NGA EHD module.

8. Conclusions

In this paper, we present the development of a sharp numerical scheme for multiphase electrohydrodynamic (EHD) flows using a high electric Reynolds number assumption. The electric potential Poisson equation contains EHD interface boundary conditions, which are implemented using the ghost fluid method (GFM). The GFM is also used to solve the pressure Poisson equation. The methods detailed here are integrated within the high order fully conservative finite difference Navier–Stokes solver of the NGA code [22] which includes state-of-the-art interface transport techniques [23,24]. Test cases with exact or approximate analytic solutions are used to assess the robustness and accuracy of the EHD modules within NGA. Finally, a charged liquid kerosene jet in quiescent air is simulated and qualitatively compared to experimental results.

Previous work by Tomar et al. [18] implemented a weighted harmonic mean (WHM) interpolation scheme to smoothen the electric properties at the interface, a coupled level set and volume-of-fluid (CLSVOF) algorithm for tracking the phase interface, and the continuum surface force (CSF) method for the electric surface forces. We develop a new representation for the interface jump conditions, employing a generalized Taylor series expansion to directly and accurately account for the discontinuities across the interface. We show that the GFM can be extended to solve the electric potential Poisson equation. The GFM is also extended to the EHD jump conditions to accurately model the strong interfacial coupling. Compared to a CSF-type approach for handling discontinuities, the application of GFM in the NGA code yields more accurate results with fewer grid points. Several test cases validate the overall methodology and demonstrate the improvements in both accuracy and efficiency compared with the current state-of-the-art for EHD modeling. The model is applied in direct numerical simulation of a charged and uncharged liquid Kerosene jet to demonstrate the robustness of the methods. The simulation results are compared to classic experiments and suggest reasonable qualitative agreement.

To explore the dynamics of EHD and its role in primary atomization, fully three-dimensional DNS of atomizing EHD liquid jets must be conducted. The complicated interplay between classical liquid disintegration mechanisms and electric disruption will require large-scale simulations to resolve. Several fundamental yet unanswered research questions will guide initial simulations of EHD atomization, such as the roles that the electric Bond number, N_E, and the electro-inertial number, N_{ei}, play in electrostatic-enhanced atomization for complex geometries and three-dimensional flows. The methodology proposed and

validated in this paper establishes a point of departure for large-scale, high-fidelity DNS of EHD atomization. Results of a detailed numerical study of electrostatic-aided atomization will serve as the focus of a future publication.

Acknowledgments

The authors gratefully acknowledge the financial support from Army Research Office Contracts W911NF-08-C-0081 and W911NF-09-C-0157 under subcontract to TDA Research, Inc. Computational resources have been provided by NSF in the form of a Teragrid TRAC allocation for high-performance computing. The authors are thankful to Dr. John S. Shrimpton, Energy Technology Research Group, University of Southampton, UK, for many fruitful discussions about EHD and this work, and for his generous contribution of figures and experimental data.

References

[1] A. Jaworek, A. Sobczyk, Electrospraying route to nanotechnology: an overview, Journal of Electrostatics 66 (3–4) (2008) 197–219.
[2] L. Rayleigh, On the equilibrium of liquid conducting masses, Philosophical Magazine, Series 5 (14) (1882) 184–186.
[3] R. Allan, S. Mason, Particle behaviour in shear and electric fields. i. Deformation and burst of fluid drops, Proceedings of the Royal Society of London. Series A 267 (1962) 45–61.
[4] A. Kelly, Electrostatic metallic spray theory, Journal of Applied Physics 47 (1976) 5264–5271.
[5] A. Kelly, The electrostatic atomization of hydrocarbons, Journal of the Institute of Energy 57 (1984) 312–320.
[6] K. Kim, R. Turnbull, Generation of charged drops on insulating liquids by electrostatic spraying, Journal of Applied Physics 47 (1976) 1964–1969.
[7] J. Melcher, G. Taylor, Electrohydrodynamics: a review of the role of interfacial shear stresses, Annual Review of Fluid Mechanics 1 (1969) 111–146.
[8] D. Saville, Electrohydrodynamic stability: effects of charge relaxation at the interface of a liquid jet, Journal of Fluid Mechanics 48 (4) (1971) 815–827.
[9] J. Shrimpton, A. Yule, Atomization, combustion, and control of charged hydrocarbon sprays, Journal of Atomization and Sprays 11 (2001) 365–396.
[10] G. Taylor, Disintegration of water drops in an electric field, Proceedings of the Royal Society of London. Series A, Mathematical and Physical Sciences (1934–1990) 280 (1382) (1965) 383–397.
[11] J. Zeleny, The electrical discharge from liquid points, and a hydrostatic method of measuring the electric intensity at their interfaces, Physical Review III (2) (1914) 69–91.
[12] J. Shrimpton, Pulsed charged sprays: application to disi engines during early injection, International Journal for Numerical Methods in Engineering 58 (2003) 513–536.
[13] J. Shrimpton, Y. Laoonual, Dynamics of electrically charged transient evaporating sprays, International Journal for Numerical Methods in Engineering 67 (2006) 1063–1091.
[14] J. Zhang, D. Kwok, A 2d lattice boltzmann study on electrohydrodynamic drop deformation with the leaky dielectric theory, Journal of Computational Physics 206 (2005) 150–161.
[15] R.T. Collins, M.T. Harris, O.A. Basaran, Breakup of electrified jets, Journal of Fluid Mechanics 588 (2007) 75–129.
[16] D. Saville, Electrohydrodynamics: the Taylor–Melcher leaky dielectric model, Annual Review of Fluid Mechanics 29 (1) (1997) 27–64.
[17] J. Baygents, N. Rivette, H. Stone, Electrohydrodynamic deformation and interaction of drop pairs, Journal of Fluid Mechanics 368 (1998) 359–375.
[18] G. Tomar, D. Gerlach, G. Biswas, N. Alleborn, A. Sharma, F. Durst, S. Welch, A. Delgado, Two-phase electrohydrodynamic simulations using a volume-of-fluid approach, Journal of Computational Physics 227 (2) (2007) 1267–1285.
[19] M. Sussman, K. Smith, M. Hussaini, M. Ohta, A sharp interface method for incompressible two-phase flows, Journal of Computational Physics 221 (2007) 469–505.
[20] J. Brackbill, D. Kothe, C. Zemach, A continuum method for modeling surface tension, Journal of Computational Physics 100 (1992) 335–354.
[21] D. Guildenbecher, Secondary Atomization of Electrostatically Charged Drops, Ph.D. Thesis, Purdue University, 2009).
[22] O. Desjardins, G. Blanquart, G. Balarac, H. Pitsch, High order conservative finite difference scheme for variable density low mach number turbulent flows, Journal of Computational Physics 227 (15) (2008) 7125–7159.
[23] O. Desjardins, V. Moureau, H. Pitsch, An accurate conservative level set/ghost fluid method for simulating turbulent atomization, Journal of Computational Physics 227 (2008) 8395–8416.
[24] O. Desjardins, H. Pitsch, A spectrally refined interface approach for simulating multiphase flows, Journal of Computational Physics 228 (5) (2009) 1658–1677.
[25] A. Castellanos, Electrohydrodynamics, Springer, 1998.
[26] G. Taylor, Studies in electrohydrodynamics. i. The circulation produced in a drop by electrical field, Proceedings of the Royal Society of London. Series A, Mathematical and Physical Sciences (1934–1990) 291 (1425) (1966) 159–166.
[27] J. Chang, A.J. Kelly, J.M. Crowley, Handbook of Electrostatic Processes, Marcel Dekker, Inc., 1995.
[28] J. Crowley, Fundamentals of Applied Electrostatics, Laplacian Press, 1986.
[29] A. Kourmatzis, J.S. Shrimpton, Electrohydrodynamics and charge injection atomizers: a review of the governing equations and turbulence, Journal of Atomization and Sprays 19 (2009) 1045–1063.
[30] W. Lehr, W. Hiller, Electrostatic atomization of liquid hydrocarbons, Journal of Electrostatics 30 (1993) 433–440.
[31] J. Shrimpton, A. Yule, Electrohydrodynamics of charge injection atomization: regimes and fundamental limits, Journal of Atomization and Sprays 13 (2003) 173–190.
[32] J. Shrimpton, A. Yule, Design issues concerning charge injection atomizers, Journal of Atomization and Sprays 14 (2004) 127–142.
[33] A. Yule, J.S. Shrimpton, W. Watkins, Electrostatically atomized hydrocarbon sprays, Fuel 74 (7) (1994) 1094–1103.
[34] R. Fedkiw, T. Aslam, B. Merriman, S. Osher, A non-oscillatory Eulerian approach to interfaces in multimaterial flows (the ghost fluid method), Journal of Computational Physics 152 (2) (1999) 457–492.
[35] O. Desjardins, Numerical Methods for Liquid Atomization and Application in Detailed Simulations of a Diesel Jet, Ph.D. Thesis, 2008.
[36] X. Liu, R. Fedkiw, M. Kang, A boundary condition capturing method for poisson's equation on irregular domains, Journal of Computational Physics 160 (1) (2000) 151–178.
[37] Y. Morinishi, T. Lund, O. Vasilyev, P. Moin, Fully conservative higher order finite difference schemes for incompressible flow, Journal of Computational Physics 143 (1998) 90–124.
[38] Y. Morinishi, O. Vasilyev, T. Ogi, Fully conservative finite difference scheme in cylindrical coordinates for incompressible flow simulations, Journal of Computational Physics 197 (2) (2004) 686–710.
[39] O. Vasilyev, High order finite difference schemes on non-uniform meshes with good conservation properties, Journal of Computational Physics 157 (2) (2000) 746–761.
[40] O. Desjardins, Detailed numerical investigation of turbulent atomization of liquid jets, in: ICLASS 2009, Vail, Colorado, 2009.
[41] O. Desjardins, Adaptive spectral refinement for accurate simulations of turbulent multiphase flows, in: ICLASS 2009, Vail, Colorado, 2009.
[42] E. Olsson, G. Kreiss, A conservative level set method for two phase flow, Journal of Computational Physics 210 (1) (2005) 225–246.
[43] S. MacLachlan, C. Oosterlee, Algebraic multigrid solvers for complex-valued matrices, SIAM Journal on Scientific Computing 30 (3) (2008) 1548–1571.
[44] J. Dendy, Black box multigrid, Journal of Computational Physics 48 (1982) 366–386.

[45] J.D. Jackson, Classical Electrodynamics, John Wiley and Sons, Inc., 1999.
[46] L.D. Landau, E.M. Lifshitz, Electrodynamics of Continuous Media, Pergamon, Oxford, 1975.
[47] K. Cheng, J. Chaddock, Deformation and stability of drops and bubbles in an electric field, Physics Letters A 106 (1984) 51–53.
[48] C. Sozou, Electrohydrodynamics of a pair of liquid drops, Journal of Fluid Mechanics 67 (1975) 339–348.
[49] N. Rivette, J. Baygents, A note on the electrostatic force and torque acting on an isolated body in an electric field, Chemical Engineering Science 51 (23) (1996) 5205–5211.
[50] B. Spatafore, B. VanPoppel, J. Daily, J. Nabity, A pulsed injection, electrostatic atomizer for small internal combustion engines, in: 45th AIAA/ASME/ASEE Joint Propulsion Conference and Exhibit, Denver, Colorado, 2009.
[51] I. Orlanski, A simple boundary condition for unbounded hyperbolic flows, Journal of Computational Physics 21 (1976) 251–269.
[52] K. Tang, A. Gomez, On the structure of an electrostatic spray of monodisperse droplets, Physics of Fluids 6 (1994) 2317–2332.